

Local Axisymmetric Simulations of Magneto-Rotational Instability in Radiation-Dominated Accretion Disks

N. J. Turner¹, J. M. Stone¹, & T. Sano¹

ABSTRACT

We perform numerical simulations of magneto-rotational instability in a local patch of accretion disk in which radiation pressure exceeds gas pressure. Such conditions may occur in the central regions of disks surrounding compact objects in active galactic nuclei and Galactic X-ray sources. We assume axisymmetry, and neglect vertical stratification. The growth rates of the instability on initially uniform magnetic fields are consistent with the linear analysis of Blaes & Socrates (2001). As is the case when radiation effects are neglected, the non-linear development of the instability leads to transitory turbulence when the initial magnetic field has no net vertical flux. During the turbulent phase, angular momentum is transported outwards. The Maxwell stress is a few times the Reynolds stress, and their sum is about four times the mean pressure in the vertical component of the magnetic field. For magnetic pressure exceeding gas pressure, turbulent fluctuations in the field produce density contrasts about equal to the ratio of magnetic to gas pressure. These are many times larger than in the corresponding gas pressure dominated situation, and may have profound implications for the steady-state vertical structure of radiation-dominated disks. Diffusion of radiation from compressed regions damps turbulent motions, converting kinetic energy into photon energy.

Subject headings: accretion, accretion disks — instabilities — MHD — radiative transfer

1. INTRODUCTION

The great decrease in specific angular momentum required to bring material from typical galactic radii to the innermost stable orbit round a central black hole indicates that accretion

¹Astronomy Department, University of Maryland, College Park, MD 20742; neal@astro.umd.edu

disks are likely present in active galactic nuclei (AGN). Direct evidence for such disks includes the kinematics of maser emission observed on parsec and sub-parsec scales in a few objects (Miyoshi et al. 1995; Gallimore et al. 1996; Greenhill, Moran, & Herrnstein 1997) and large asymmetries in the 6.4 keV iron fluorescence line which may be due to orbital motion in a general relativistic potential (Tanaka et al. 1995; Fabian et al. 2000). Some Galactic X-ray sources are associated with collimated relativistic jets, suggesting disks occur around stellar-mass compact objects also (Mirabel & Rodriguez 1999). In a few cases, light curves during eclipses by a companion star indicate an extended structure about the compact object (Parmar et al. 1986; Orosz & Bailyn 1997).

One of the major uncertainties regarding disk accretion is how the angular momentum is lost from incoming material. A leading candidate mechanism is the magneto-rotational instability (MRI), whose importance for accretion disks was pointed out by Balbus & Hawley (1991). The MRI is driven by outward radial transport of angular momentum along magnetic field lines sheared by differential orbital motion. In most previous studies of the instability, effects of radiation have been neglected. It has been found that provided dissipation of the field is negligible and magnetic pressure is much less than gas pressure, the fastest linear mode of the instability grows at near three-quarters the orbital angular frequency Ω , independent of the field orientation. This mode has a wavelength along the direction parallel to the magnetic field of approximately $2\pi v_A/\Omega$, where v_A is the Alfvén speed (Balbus & Hawley 1998). In magnetohydrodynamical (MHD) simulations of the non-linear development with imposed axisymmetry, the instability develops from an initially uniform vertical magnetic field into an exponentially-growing two-channel flow. From spatially-varying fields with zero net vertical flux, short-lived turbulence is produced (Hawley & Balbus 1992). In three-dimensional MHD calculations, the MRI leads to outward angular momentum transport by long-lasting turbulence with velocity fluctuations smaller than or comparable to the sound speed (Hawley, Gammie, & Balbus 1995, 1996). An initially weak magnetic field grows to a saturated level which is sustained for many orbits despite effects of disk stratification (Brandenburg et al. 1995; Stone et al. 1996).

A second major issue regarding disk accretion is how the released gravitational energy is converted into radiation. The energy released in reaching the innermost stable orbit round a black hole is a significant fraction of the rest energy of the incoming material. In parts of the accretion disk, radiation pressure may therefore greatly exceed the ordinary gas pressure due to thermal motions of material particles (Shakura & Sunyaev 1973). If the released energy is placed in the gas through viscous or resistive dissipation, radiation may be produced by thermal emission provided the absorption optical depth through the disk is sufficient. Alternatively if the released energy is placed in turbulent motions, the kinetic energy might be converted directly into photon energy by radiative damping. This occurs

when work is done on the radiation in compressing a part of the flow, and photons diffuse away from the region of higher energy density. For linear compressive MHD waves in the absence of rotation, damping may be rapid when the wave period is longer than the time for photons to diffuse across the wavelength (Agol & Krolik 1998). During linear growth of the axisymmetric MRI, radiative damping may be strong when in addition the pressure in the azimuthal component of the magnetic field exceeds the gas pressure (Blaes & Socrates 2001).

In this paper we investigate the effects of radiation on the non-linear development of the MRI. As in the first such studies in the gas pressure dominated regime (Hawley & Balbus 1991, 1992), we assume axisymmetry, neglect vertical stratification, and consider a small patch in the interior of the disk. The dependence of the magnetic stresses on the gas and radiation pressures cannot be determined from such axisymmetric calculations lacking sustained dynamo activity. However, radiation diffusion and the inclusion of magnetic pressures exceeding gas pressure may lead to new effects. The equations solved and numerical method used are described in § 2, the initial conditions and computational domain in § 3. Results from the linear growth phase are compared against linear analyses in § 4. Effects of radiation on the channel flow which develops from initially uniform vertical fields are outlined in § 5. Radiation effects in the decaying turbulence on fields with zero net vertical flux are examined in § 6, and the significance of the results for the structure of accretion disks is discussed in § 7. A summary and conclusions are in § 8.

2. EQUATIONS SOLVED AND NUMERICAL METHODS

The radiation magnetohydrodynamic equations solved are written in a frame comoving with the radiating fluid, in cgs units. Relativistic effects are neglected. Terms to order unity in v/c are included, and local thermodynamic equilibrium is assumed. The equations are

$$\frac{D\rho}{Dt} + \rho \nabla \cdot \mathbf{v} = 0, \quad (1)$$

$$\rho \frac{D\mathbf{v}}{Dt} = -\nabla p + \frac{1}{4\pi} (\nabla \times \mathbf{B}) \times \mathbf{B} + \frac{1}{c} \chi \rho \mathbf{F}, \quad (2)$$

$$\rho \frac{D}{Dt} \left(\frac{E}{\rho} \right) = -\nabla \cdot \mathbf{F} - \nabla \mathbf{v} : \mathbf{P} + \kappa \rho (4\pi B - cE), \quad (3)$$

$$\rho \frac{D}{Dt} \left(\frac{e}{\rho} \right) = -p \nabla \cdot \mathbf{v} - \kappa \rho (4\pi B - cE), \quad (4)$$

$$\mathbf{F} = -\frac{c\lambda}{\chi\rho} \nabla E, \quad (5)$$

and

$$\frac{\partial \mathbf{B}}{\partial t} = \nabla \times (\mathbf{v} \times \mathbf{B}) \quad (6)$$

(Mihalas & Mihalas 1984; Stone, Mihalas, & Norman 1992). Here the convective derivative D/Dt is equivalent to $\partial/\partial t + \mathbf{v} \cdot \nabla$. The dependent quantities ρ , e , \mathbf{v} , and p are gas mass density, energy density, velocity, and scalar isotropic pressure, respectively, and \mathbf{B} is magnetic field. The radiation is described by E , \mathbf{F} , and \mathbf{P} , the total frequency-integrated radiation energy density, flux, and pressure tensor, respectively. Total opacity χ is the sum of absorption κ and scattering σ . The opacities have units of cross-section per unit mass, and are treated as independent of photon frequency. Emission proportional to the black-body rate $B = \sigma_B T_g^4/\pi$ is assumed for the material component, where σ_B is the Boltzmann constant and $T_g = p\mu/(\mathcal{R}\rho)$ the gas temperature. The gas constant is written \mathcal{R} , and the dimensionless mean mass per particle μ is taken to be 0.6. An ideal-gas equation of state is assumed, and the gas pressure is related to the gas energy density by $p = (\gamma - 1)e$ with $\gamma = 5/3$. The temperature of the radiation field is computed by $T_r = (E/a_R)^{1/4}$, where $a_R = 4\sigma_B/c$. Additional terms in the gas momentum equation 2 due to tidal and rotating frame forces are discussed in § 3.

The equations are integrated using the ZEUS MHD code (Stone & Norman 1992a,b). Shocks are captured with a standard quadratic artificial viscosity (von Neumann & Richtmyer 1950). In ZEUS-2D, the azimuthal component of the magnetic field is normally evolved as a passive scalar, as described by Stone & Norman (1992b). However, we have found that this treatment results in a changing net azimuthal magnetic flux, whereas the azimuthal component of the field evolution equation 6 integrated over the periodic shearing sheet indicates that azimuthal flux ought to be conserved when radial flux is zero (Hawley, Gammie, & Balbus 1995). In trial calculations of the development of magnetized turbulence in a shearing-sheet configuration, azimuthal flux varied by up to 20% when azimuthal field was evolved as a scalar, and by a fraction of a percent when all components were treated using the method of characteristics with constrained transport (MOC-CT; Stone & Norman 1992b). The three components are advanced together using MOC-CT in the remainder of the calculations reported here.

The radiation terms in the equations are treated using the flux-limited radiation diffusion (FLD) module described by Turner & Stone (2001). In the FLD approximation (Levermore & Pomraning 1981), neither a radiation momentum equation nor a radiation transfer equation is explicitly solved. The flux is assumed to be $\mathbf{F} = -D\nabla E$, where the radiation diffusion coefficient $D = c\lambda/(\chi\rho)$ incorporates a flux-limiter $0 < \lambda \leq 1/3$. The limiter is chosen according to the prescription of Levermore & Pomraning (1981) so as to ensure the flux in optically-thin regions obeys the causality constraint $|\mathbf{F}| \leq cE$. The radiation pressure tensor

$\mathbf{P} = fE$ is obtained using an Eddington tensor \mathbf{f} whose components depend on ∇E , rather than on full solutions of the radiation transfer equation. In the majority of the calculations discussed in this paper, each grid zone is optically-thick. Under these conditions the flux-limiter is very close to $1/3$, the radiation pressure is isotropic and described by the scalar P , and the FLD method is equivalent to a two-temperature diffusion approximation.

3. GRID AND INITIAL CONDITIONS

We use the shearing-sheet approximation (Hawley & Balbus 1992). A small patch of the disk is represented in local corotating Cartesian coordinates (x, y, z) . At time t the origin of the local coordinates lies at $(R_0, \Omega_0 t, 0)$ in global inertial cylindrical coordinates (R, ϕ, z) . The local coordinates rotate with the Keplerian orbital frequency $\Omega_0 = (GM/R_0^3)^{1/2}$ appropriate for a central mass M and gravitational constant G . Symmetry along the y -axis or direction of orbital motion is assumed. The radial component of the gravitational force due to the central mass is included in the x -component of the gas momentum equation 2 through a tidal term $3\rho\Omega_0^2 x$ on the right-hand side. The Coriolis force due to the rotation of the frame is incorporated through a term $-2\rho\Omega_0 \hat{\mathbf{z}} \times \mathbf{v}$, where $\hat{\mathbf{z}}$ is a unit vector along the rotation axis. The vertical component of the gravitational force is not included. Initially the orbital or y -component of the velocity varies linearly with x in an expansion of the Keplerian rotation curve about R_0 , while the x - and z -components are small or zero. Mass density and gas and radiation energy densities are uniform, and gas and radiation are in thermal equilibrium. The x - and z - boundaries are taken to be periodic, except that y -velocity is offset across the x -boundaries according to the differential orbital motion. The grid zones are square and evenly-spaced.

Steady-state conditions might occur in an accretion disk when gains and losses of both magnetic and radiation energy balance. In the present axisymmetric calculations, sustained dynamo action is not expected and surface losses are ignored, so the outcome is largely fixed by the starting conditions. We explore several initial field strengths and geometries, and set the gas and radiation pressures and the diffusion rate by choosing initial mass and energy densities from a standard time-steady, optically-thick viscous accretion disk model (Shakura & Sunyaev 1973). In this model, energy loss by radiative diffusion through the disk surfaces is assumed to balance vertically-integrated dissipation at each radius, and accretion is due to an effective viscous shear stress proportional to local radiation plus gas pressure $P + p$ with constant of proportionality α . The half-thickness of the disk H is determined by vertical hydrostatic balance, and is independent of radius R in the radiation-dominated region because the vertical components of the forces due to gravity and radiation both scale as R^{-3} .

Estimates of the surface density Σ and midplane radiation acoustic speed $c_r = (\frac{4}{3}P/\rho)^{1/2}$, gas acoustic speed $c_g = (\gamma p/\rho)^{1/2}$, and opacities are obtained neglecting relativistic corrections and assuming matter and radiation are in local thermodynamic equilibrium. The opacities used are due to electron scattering, $\sigma_{\text{es}} = 0.4 \text{ cm}^2 \text{ g}^{-1}$, and free-free absorption, $\kappa_{\text{ff}} = 10^{52} \rho^{9/2} e^{-7/2} \text{ cm}^2 \text{ g}^{-1}$. For the range of parameters considered here, Comptonization and bound-free opacities have little effect on interior structure of an α -disk (Hubeny et al. 2001). Results are shown in figure 1 for a central mass $M = 10^8 M_\odot$, accretion rate 10% of the Eddington rate $\dot{M}_E = 2.65 \times 10^{-9} (M/M_\odot) \eta^{-1} M_\odot \text{ yr}^{-1}$ with luminous efficiency $\eta = 0.1$, and α parameter 0.01. Starting values for the majority of the calculations are taken from the radius marked A, where radiation acoustic speed is ten times gas acoustic speed. This location lies at 67.8 gravitational radii $r_G = GM/c^2$. The Keplerian orbital speed here is $0.12 c$, the radiation acoustic speed is 2.2% of the Keplerian speed, and radiation pressure is 125 times gas pressure. The power law index in the equation of state of gas plus radiation is therefore close to $4/3$. For some additional calculations, initial conditions are taken from location B at $392 r_G$, where the two acoustic speeds are equal. The radiation pressure is 1.25 times the gas pressure, so that this location is near the outer edge of the radiation-dominated region. Under these conditions the power law index in the combined equation of state is expected to be 1.4 (Mihalas & Mihalas 1984, p. 320), intermediate between those for radiation and gas separately. In numerical calculations with location B initial conditions, acoustic vibrations in the absence of radiation diffusion have speeds consistent with the expected equation of state. The initial conditions taken from the midplane at locations A and B are listed in table 1. The effective absorption optical depth of the disk depends on the distances traveled by photons scattered multiple times between emission and escape, and is

$$\tau^* = \Sigma \sqrt{\sigma \kappa}. \quad (7)$$

As may be seen from table 1, the initial disk model is effectively optically thick to both free-free absorption and electron scattering at the two locations considered. Local absorption and emission of photons bring gas and radiation into equilibrium in a time

$$t_{\text{eqm}} \approx \frac{e}{c \kappa \rho E}. \quad (8)$$

We have verified by numerical integration of the coupled gas and radiation energy equations 3 and 4 with $\mathbf{v} = \mathbf{F} = \mathbf{0}$ that equation 8 approximately describes the damping of gas and radiation pressure perturbations at locations A and B. As indicated in table 1, the equilibration time is orders of magnitude shorter than the orbital period at both locations. When the physical equilibration time is shorter than the numerical timestep, the implicit differencing scheme used in the FLD module remains stable, and gas and radiation are brought into thermal equilibrium in a few timesteps (Turner & Stone 2001). Finally, we have checked

that the initial conditions are dynamically stable when no magnetic field is present. Applied radial and azimuthal velocity perturbations lead to epicyclic oscillations at frequency Ω_0 .

The values of ρ , e , and E from the disk model listed in table 1 are inserted as initial conditions in radiation MHD simulations described in the remainder of this article. These simulations include no viscous accretion stress, and no viscous heating apart from the standard artificial viscosity described in § 2. The only source terms in the azimuthal component of the equation of motion 2 are the Lorentz and Coriolis forces.

4. COMPARISON WITH LINEAR ANALYSES

In this section we examine the linear growth of the MRI. Results from numerical calculations are compared against analytic estimates for magnetic fields which are initially vertical, vertical plus azimuthal, and radial. These comparisons may reveal shortcomings of our numerical techniques.

Blaes & Socrates (2001) considered the case where radiation pressure is important, absorption opacity is zero, and the initial magnetic field has a vertical and possibly an azimuthal component. When stratification is neglected, the dispersion relation obtained by an axisymmetric WKB analysis is their equation 39. The unstable modes of the MRI are found to be unchanged by radiation diffusion when the field is initially vertical. Numerical results for this geometry are discussed in § 4.1. When the initial azimuthal magnetic pressure exceeds the gas pressure, the growth rates are reduced if the time for radiation to diffuse across the vertical wavelength is shorter than the orbital period. Numerical results in several such cases are presented in § 4.2.

For initially radial magnetic fields, no linear analysis including effects of radiation is presently available. In the case where gas pressure is greater than magnetic pressure and radiation effects are negligible, the general dispersion relation from Balbus & Hawley (1991) indicates that the fastest-growing incompressible axisymmetric mode has radial wavelength approximately $2\pi v_A/\Omega_0$, vertical wavelength asymptotically zero, and growth rate near $\frac{3}{4}\Omega_0$. Some numerical results with and without radiation are discussed in § 4.3.

Growth rates in the simulations below are measured by computing the time rate of change in the Fourier power spectrum components of the x -velocity distribution, about one orbital period before the end of the linear growth stage. The velocity distribution is sampled every 0.1 orbital period.

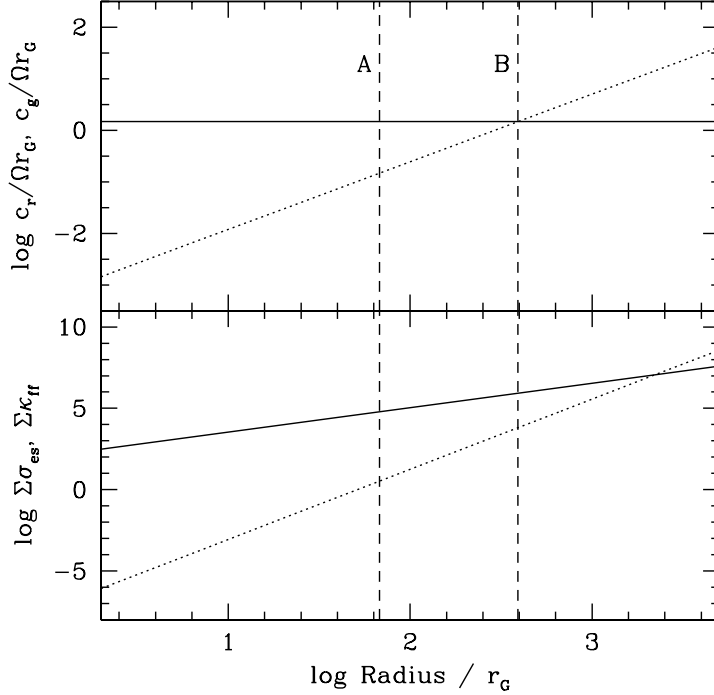


Fig. 1.— Standard initial conditions are taken from this Shakura-Sunyaev model disk accreting into a $10^8 M_\odot$ black hole at 10% of the Eddington rate, with luminous efficiency 0.1 and $\alpha = 0.01$. The horizontal axis is distance from the center of mass in gravitational radii $r_G = GM/c^2$. In the upper panel are shown the disk half-thicknesses in units of r_G , corresponding to support by radiation pressure (solid) and gas pressure (dotted). In the lower panel are the total optical depths due to electron scattering (solid) and free-free absorption (dotted). Dashed vertical lines indicate the radii where the local midplane radiation acoustic speed is ten times greater than the gas acoustic speed (labeled A) and equal to the gas acoustic speed (labeled B). Initial conditions for most of the simulations are taken from one of these two locations.

4.1. Uniform Vertical Magnetic Field

Initial conditions and orbital frequency for these calculations are extracted from location A in the disk model discussed in § 3. The magnetic field is initially vertical, with strength chosen so the Alfvén speed $v_A = |\mathbf{B}| / \sqrt{4\pi\rho}$ is equal to the gas acoustic speed. The height and width of the computational domain are set to the vertical wavelength of the mode to be examined, and the domain is divided into 64^2 zones. The x -velocity is perturbed with a sinusoidal variation in z having the wavelength of the mode. Its initial amplitude is smaller than the Keplerian speed at R_0 by a factor 10^8 , and smaller than the radiation acoustic speed by a factor 2.2×10^6 . Both electron scattering and free-free absorption opacities are included.

Modes with wavelengths 2/3, 1, and 2 times the characteristic MRI wavelength $2\pi v_A / \Omega_0$ have growth rates differing by less than 1% from those predicted using the Blaes & Socrates (2001) dispersion relation, their equation 39. The three modes grow at similar rates with the free-free absorption opacity set to zero, and with the scattering opacity instead reduced a factor 100; under these latter conditions, radiation diffuses across the domain in less than an orbit. These results support the conclusion of Blaes & Socrates (2001) that on initially vertical fields in a scattering medium, the spectrum of unstable modes of the MRI is unaffected by radiation diffusion. The small absorption opacity also has little effect on the modes.

4.2. Uniform Vertical Plus Azimuthal Magnetic Field

For the first set of calculations in this section, the initial conditions are identical to those in § 4.1 except that a large azimuthal component is added to the magnetic field. The total Alfvén speed is equal to the radiation acoustic speed, and is ten times the vertical Alfvén speed $v_{Az} = B_z / \sqrt{4\pi\rho}$. The Blaes & Socrates (2001) dispersion relation indicates that the fastest axisymmetric MRI mode in this situation has wavelength near $2\pi v_{Az} / \Omega_0$. Modes with wavelengths 0.78, 1.16, and 2.33 times this characteristic value are examined.

In the other calculations in this section, the diffusion rate is varied by choosing initial conditions from time-steady viscous accretion disk models with different values of the α parameter. For each diffusion rate, the expected dependence of growth rate on wavenumber is shown by a dotted curve in figure 2. Growth rates measured in the simulations are indicated by open circles. Overall, the agreement between the linear analysis and the numerical results is within about 1%. Use of the same numerical method in studying the non-linear development therefore seems worthwhile.

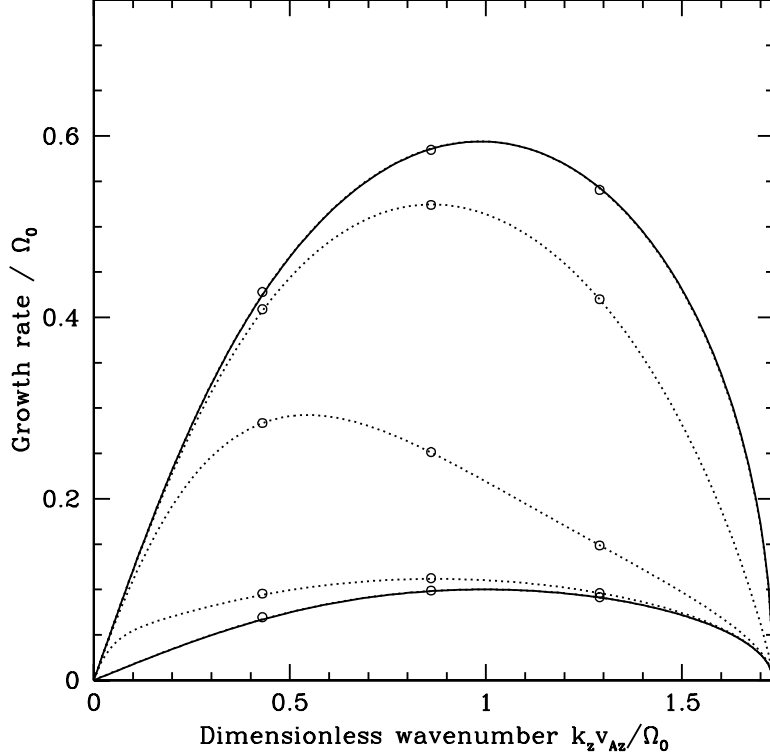


Fig. 2.— Linear growth rate of the MRI versus wavenumber, on an initially uniform magnetic field. The field has azimuthal and vertical components, the vertical being 10% of the magnitude. Growth rate is plotted against the product of vertical wavenumber k_z and vertical Alfvén speed v_{Az} . Both axes are labeled in units of the orbital frequency Ω_0 . Axisymmetry is assumed, and the radial wavenumber k_x is zero. Solid curves: limits in which diffusion is very slow (upper) and very fast (lower). Dotted curves: solutions of the Blaes & Socrates (2001) dispersion relation including radiation, with diffusion rate increasing from top to bottom. Total Alfvén speed is equal to radiation acoustic speed, and is ten times gas acoustic speed. The dotted curve peaking near growth rate $0.5\Omega_0$ corresponds to the diffusion rate at location A in the model disk discussed in § 3. The uppermost dotted curve, which overlaps the upper solid curve, is for a diffusion rate 100 times slower. The lower curves are for diffusion rates 10, 100, and 10^4 times faster. The lowest dotted curve overlaps the lower solid curve. Circles indicate growth rates measured in the linear phases of corresponding numerical simulations.

4.3. Uniform Radial Magnetic Field

We first check growth rates in a simulation without radiation effects against those predicted using the dispersion relation from Balbus & Hawley (1991). Solution of their equation 2.17 indicates that on radial field the fastest-growing mode has zero vertical wavelength. To locate the fastest mode present on the grid, random perturbations are applied to the x - and z -velocities. Each component has probability distribution uniform between $+$ and -10^{-8} times the Keplerian speed at R_0 . Initial density is as in § 4.1, and gas pressure is set to the sum of the gas and radiation pressures in § 4.1. Alfvén speed is set to 10% of its value there, so that $\beta = p/(|\mathbf{B}|^2/8\pi)$ is 15 120. The grid consists of 64×64 zones, and the domain height and width are twice the characteristic wavelength $2\pi v_A/\Omega_0$.

The mode which grows fastest in the linear stage has two wavelengths across the width of the box and 32 in the height, and grows at $0.726\Omega_0$. The growth rate expected for this mode from the linear analysis is $0.7478\Omega_0$. Although the vertical wavelength is two grid zones and the mode is grossly under-resolved, the measured growth rate is only slightly less than the expected value.

Diffusion of radiation is likely to be rapid in configurations with such short vertical wavelengths. If radiation pressure support is lost, the velocity pattern of the perturbation may acquire a non-zero divergence when shear acting on radial magnetic field produces an azimuthal field exceeding equipartition with the gas. Such compressible motions are associated with reduced growth rates when radiation effects are unimportant (Blaes & Balbus 1994; Kim & Ostriker 2000).

In a second calculation, with the same initial magnetic field as above but including a radiation energy density as in § 4.1 so the ratio of gas to magnetic pressure $\beta = 120$, we find that the measured growth rate declines below $0.1\Omega_0$ over several orbits as azimuthal magnetic pressure grows larger than gas pressure. To allow measurement of the weak-field linear growth rate, an initial magnetic field ten times smaller is selected for a third calculation. The size of the domain is reduced to twice the new characteristic MRI wavelength. In this case β is initially 12 000, and equipartition between field and gas is not reached for several orbits. The fastest-growing mode observed has two wavelengths in the domain width and 28 in the height, and grows at $0.721\Omega_0$. The differences between the second and third calculations indicate that radiation diffusion can greatly reduce the growth rate of the MRI on initially radial magnetic field, when the magnetic pressure exceeds the gas pressure.

5. NON-LINEAR EVOLUTION ON UNIFORM VERTICAL MAGNETIC FIELD

In the non-linear regime, the axisymmetric MRI leads to development of exponentially-growing channel solutions when the initial field has a net vertical flux and radiative and resistive effects are slight (Hawley & Balbus 1992; Goodman & Xu 1994). Any smaller-scale features undergo an inverse cascade until the domain is filled by an inward-moving and an outward-moving channel, separated by regions of strong radial and azimuthal magnetic field. We have carried out calculations of this phenomenon with and without radiation effects, using identical initially uniform vertical fields. Initial mass and energy densities for the case with radiation are as at location A in the disk model of § 3, and the field strength is such that Alfvén speed equals gas acoustic speed. For the case without radiation, the initial gas energy density is chosen to give the same total pressure. The width and height of the domain are twice the characteristic wavelength of the MRI. A radial velocity perturbation independent of x is applied. Its vertical wavelength is equal to the characteristic wavelength, and its amplitude is 10^{-4} times the Keplerian orbital speed at R_0 .

Results at the start of the non-linear stage are shown in figure 3. In the case with radiation, diffusion from the compressed layers into the lower-density, magnetically-dominated layers leads to faster compression and a weaker temperature contrast. Oppositely-directed radial and azimuthal magnetic fields are brought into a single grid zone in the compressed layer somewhat earlier in the case with radiation, and rapid numerical reconnection of the field follows.

6. NON-LINEAR EVOLUTION ON FIELD WITH ZERO NET VERTICAL FLUX

In previous axisymmetric calculations without radiation, the linear development of the MRI on a magnetic field with zero net vertical flux is followed by a period of turbulence. The fluctuations die away over several orbits as vertical field of opposing signs is brought together and lost from the calculation through numerical dissipation (Hawley & Balbus 1992). In this section we describe the results of a series of simulations in which the strengths of the radiation effects are varied to determine how they affect the transitory turbulence. Throughout, the domain average of a quantity Q is indicated $\langle Q \rangle$. Time-averaged values are indicated by a second pair of angle braces $\langle\langle Q \rangle\rangle$.

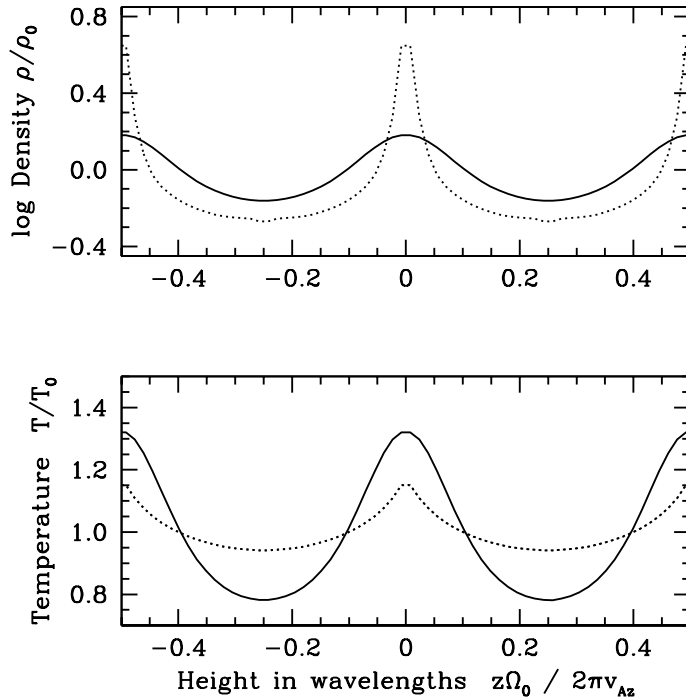


Fig. 3.— Non-linear development of the MRI from an initially uniform vertical magnetic field, as discussed in § 5. Variation of density (upper) and temperature (lower) with height at $x = 0$ is shown at the time when the pressure of the magnetic field perturbation first exceeds initial gas plus radiation pressure. Only the central wavelength of the disturbance is plotted. Results from a calculation including radiation pressure are shown by dotted curves. Those from a calculation without radiation, having initial gas pressure increased to give the same total pressure, are shown by solid curves. There are 64 grid zones per wavelength in both cases.

6.1. Canonical Simulation

The uniform initial values of the density and gas and radiation energy densities for the canonical simulation are taken from location A as described in § 3. The initial magnetic field is given a large azimuthal component because this configuration leads to strong effects of radiation diffusion during the linear growth. The strength of the initial field B_0 is made independent of position and the radial component is set to zero, so that there are no unbalanced forces. The field direction varies sinusoidally with x . At grid center $x = 0$, the field is inclined $\theta = +5.7^\circ$ from azimuthal, so that the vertical component $B_z = 0.1B_0$. At the boundaries $x = \pm L/2$, the field is inclined -5.7° , and at $x = \pm L/4$, it is entirely azimuthal. The domain has height and width L . The components of the field are

$$B_z = B_0 \sin \theta \cos(2\pi x/L), \quad (9)$$

$$B_y = (B_0^2 - B_z^2)^{1/2}, \quad (10)$$

and

$$B_x = 0, \quad (11)$$

with $\sin \theta = 0.1$. The azimuthal component B_y is everywhere positive. Field strength B_0 is chosen so Alfvén speed is equal to radiation acoustic speed and is ten times gas acoustic speed. The pressures due to radiation, magnetic field, and gas are in the ratio 125 : 83.3 : 1. Each zone is given small random x - and z -velocities. The probability distribution for each component of the velocity is linear between -10^{-4} and 10^{-4} times the Keplerian speed at the central radius R_0 . The domain size L is set to twice the characteristic wavelength of the axisymmetric MRI $2\pi v_{Az}/\Omega_0$ measured at grid center, and the grid consists of 128^2 zones. The domain height is 51% of the thickness of the disk model from which the initial conditions were selected. In the initial state, the time for radiation acoustic waves to cross the domain is 0.2 orbits, and photons diffuse across the domain in $L^2/D = 50$ orbits.

After about one orbit during which the energy in the initial velocity perturbations is redistributed among gas, radiation, magnetic, and kinetic energies, the simulation proceeds through three stages, as shown in figure 4. During the linear stage, covering the remainder of the first 4.1 orbits, a mode with vertical wavelength equal to the characteristic MRI wavelength grows exponentially at about half the orbital frequency. This mode has nulls at $x = \pm L/4$, where the vertical component of the field is zero. The linear stage ends when the radial field resulting from the instability is comparable in strength to the initial vertical field. Inward and outward moving flows then collide, and the simulation enters the turbulent stage. We choose to place the beginning of the turbulent stage at the time when the energy in the radial component of the field first peaks. The turbulence decreases in intensity as the energy in the vertical component of the field falls due to numerical losses. After about 17 orbits, the

Maxwell stress drops below 1% of its peak value, and the Reynolds stress oscillates about zero with twice the epicyclic frequency. The flow remains in this third, almost quiescent stage until the end of the simulation at 30 orbits. In the other simulations described below, the flow passes through the same three stages. The durations of the linear and turbulent stages are different in each case. In each simulation we focus on the period from 2 to 6 orbits after the start of the turbulent stage, when transients reflecting the linear development have been largely erased, and the fluctuations remain strong.

6.2. Turbulent Fluctuations

The density variations during the turbulent stage in the canonical simulation are larger than in similar gas pressure dominated calculations. The RMS fluctuation averaged from 2 to 6 orbits after the onset of turbulence is 110% of the mean density (figure 4, center right panel). On average, half the mass is contained in the 18% of the volume where densities are greatest. Throughout the same period the largest density in the domain is about 200 times the smallest. Overdense regions form and disperse often. Typically a clump is present about one orbit before being destroyed either in a collision with another clump, or in passing through a region of shear in the turbulence.

Density fluctuations of similar magnitude are seen in versions of the canonical simulation with the domain size extended to 2.5 and 4 characteristic MRI wavelengths, and 160^2 and 256^2 zones, respectively. These calculations are listed in table 2 as R2.5w and R4w. From these results we infer the large densities are not due solely to the limited number of linearly unstable modes present in the canonical domain. There are three linear modes with $k_x = 0$ whose vertical wavelengths evenly divide the canonical domain height, whereas six such modes are present in the double-size calculation R4w.

Similar density fluctuations are also seen in a double-resolution version of the canonical simulation R1d2 having 256^2 zones. The highest and lowest densities are about the same in the canonical and double-resolution calculations, and the densest regions have similar physical sizes such that radiation diffuses out of them in approximately an orbital period. It is likely that the densest regions are adequately resolved in the canonical calculation.

All of these results may be compared against two versions of the canonical calculation without radiation. In the first, labeled N11 in table 2, the initial gas pressure is unchanged from the canonical calculation and is 1.2% of the magnetic pressure. Linear growth rates in this situation are as on the lower solid curve in figure 2. During the turbulent stage in run N11, mean gas pressure increases monotonically owing to compression and artificial viscous

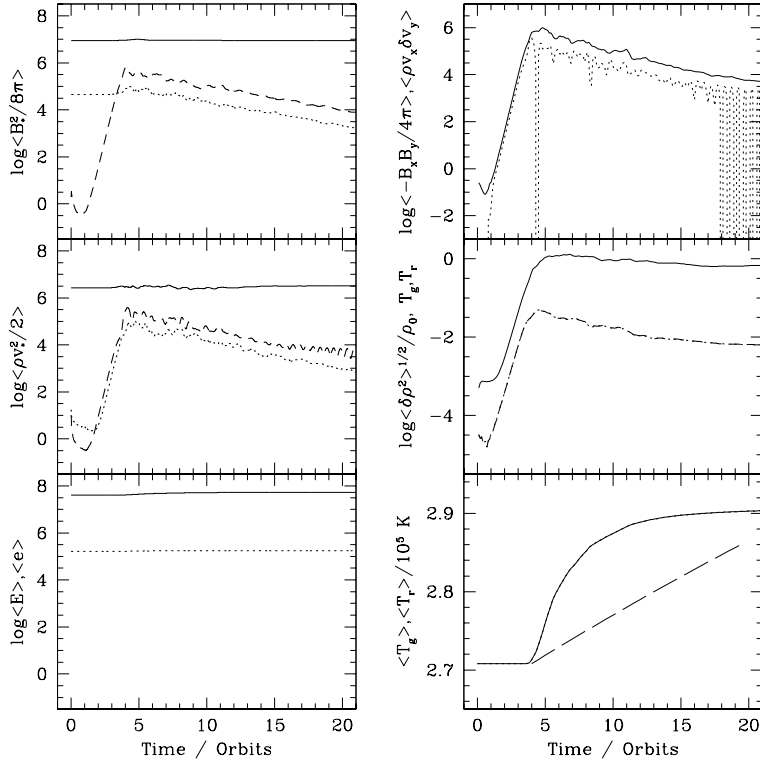


Fig. 4.— Time history of domain-averaged quantities in the canonical simulation described in § 6.1. Magnetic and kinetic energy densities measured in the local frame are shown in the top two panels on the left. The energies in the x -, y -, and z -components are indicated by dashed, solid, and dotted lines, respectively. Radiation (solid) and gas (dotted) energy densities are plotted on the same scale in the lower left panel. At upper right are the Maxwell (solid) and Reynolds (dotted) accretion stresses. In the center right panel are the RMS fluctuations in density (solid), gas temperature (dotted) and radiation temperature (dashed). At lower right are the temperatures of the radiation (solid) and gas (dotted, hidden by solid line). The heating which would result from the energy release rate assumed in the initial disk model at location A is indicated by a long-dashed line.

heating accompanying shocks. The gas pressure time-averaged from 2 to 6 orbits after the start of turbulence is 14% of the corresponding magnetic pressure. The time-averaged RMS density fluctuation in this case is 68%, and the mean ratio of the largest density to the smallest is 80. These are almost as large as in the canonical simulation.

In the second calculation without radiation, the radiation pressure is replaced by an equal amount of additional gas pressure, so initially the gas pressure is 1.5 times the magnetic pressure. This calculation is labeled N16 in table 2. Linear growth rates under these conditions lie near the upper solid curve in figure 2. During the turbulent stage in run N16, the ratio of time-averaged gas to magnetic pressure is 1.69. This is comparable to the ratio 1.79 in the canonical simulation, of time-averaged gas plus radiation pressure to magnetic pressure. The time-averaged RMS density fluctuation in N16 is 8.4%, and the typical density range is a factor two, about two orders of magnitude less than in the canonical simulation.

Snapshots of the density distributions in the three calculations 3 orbits after the start of the turbulent stage are shown in figure 5. A similar relationship between the density fluctuations in the three calculations extends over the whole averaging period. Histograms of the density, time-averaged from 2 to 6 orbits after the onset of turbulence, are shown in figure 6. The two calculations with large density fluctuations show quite different linear growth rates. The canonical simulation enters the turbulent stage after 4.1 orbits, while the version with the same initial gas pressure but without radiation reaches a similar amplitude only after 18.8 orbits. The linear growth rate does not appear to be a good predictor of the strength of the density fluctuations in the turbulent stage in these axisymmetric calculations.

Total pressure is almost uniform in the canonical simulation. Regions of higher density and gas and radiation pressures correspond to regions of lower magnetic pressure. The time-averaged RMS fluctuation in magnetic pressure is 13 times larger than the corresponding fluctuation in gas pressure, and is roughly equal to the fluctuation in gas plus radiation pressure. In the two calculations N11 and N16 without radiation, the gas and magnetic pressure fluctuations are roughly equal. Apparently in the canonical calculation, diffusion does not completely decouple gas and radiation over a dynamical time, and radiation pressure gradients provide some support against magnetic forces.

The fractional RMS gas temperature fluctuations in the canonical simulation are 30 to 100 times smaller than the density fluctuations (figure 4, center right panel). By contrast, in both of the calculations without radiation, temperature fluctuations are comparable to density fluctuations, as expected for adiabatic evolution. In the canonical simulation the radiation energy density is more smoothly distributed than the gas energy density, owing to diffusion of the radiation with respect to the gas. Diffusion is faster in the turbulent stage than initially, due to the concentration of most of the opacity in small dense regions. The

Table 1. Initial conditions

Location	A	B
R/r_G	67.8	392
c_r/c_g	10	1
P/p	125	1.25
τ_{es}	6.2×10^4	8.6×10^5
τ_{ff}^*	4.5×10^2	7.5×10^4
$t_{\text{eqm}}\Omega_0/2\pi$	1.2×10^{-6}	4.6×10^{-9}
$\rho/\text{g cm}^{-3}$	2.89×10^{-9}	4.02×10^{-8}
$T_g = T_r/\text{K}$	2.71×10^5	1.40×10^5
$e/\text{erg cm}^{-3}$	1.63×10^5	1.17×10^6
$E/\text{erg cm}^{-3}$	4.07×10^7	2.93×10^6

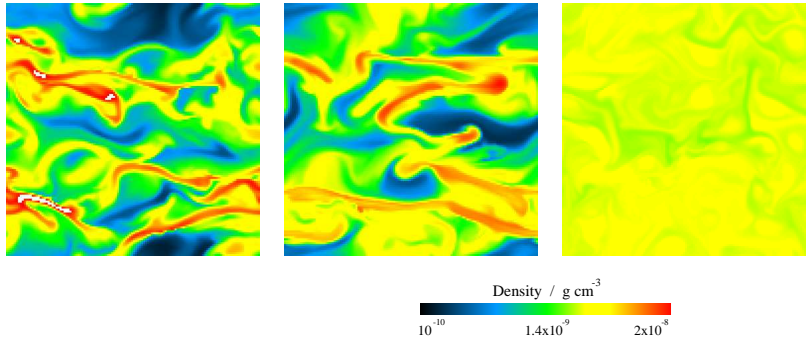


Fig. 5.— Snapshots of the density distribution three orbits after turbulence begins, in the canonical simulation R1 (left) and calculations without radiation having the same initial gas pressure (N11, center) and the same initial total pressure (N16, right). A common logarithmic scale is used. The radial coordinate x increases to the right in each panel, and z increases upwards.

Table 2. Simulations at location A with strong azimuthal field.

Label	Name	$L/(2H)$	Zones	$\log \mathbf{B} / B_0$	$\sigma / \sigma_{\text{es}}$	$\log \langle \langle \rho_{\text{max}} / \rho_{\text{min}} \rangle \rangle$
R1	Canonical	0.51	128^2	0.0	1	2.30
R2		0.16	128^2	−0.5	1	1.32
R3		0.051	128^2	−1.0	1	0.46
R4		0.016	128^2	−1.5	1	0.081
R5		0.0051	128^2	−2.0	1	0.0061
R2.5w	2.5-wavelength	0.64	160^2	0.0	1	2.25
R4w	4-wavelength	1.02	256^2	0.0	1	1.79
R1d2	Double-resolution	0.51	256^2	0.0	1	2.20
R1t	Timesteps/10	0.51	128^2	0.0	1	2.22
R1b	Negative- B_y	0.51	128^2	0.0	1	1.95
R1v	Artificial viscosity/10	0.51	128^2	0.0	1	1.99
R1s	Very high opacity	0.51	128^2	0.0	10^4	0.287
R6	High-opacity	0.51	128^2	0.0	100	0.276
R7		0.16	128^2	−0.5	100	0.150
R8		0.051	128^2	−1.0	100	0.113
R9		0.016	128^2	−1.5	100	0.039
R10		0.0051	128^2	−2.0	100	0.0061
N11	Same gas pressure	0.51	128^2	0.0	...	1.90
N12		0.16	128^2	−0.5	...	0.90
N13		0.051	128^2	−1.0	...	0.32
N14		0.016	128^2	−1.5	...	0.200
N15		0.0051	128^2	−2.0	...	0.085
N16	Same total pressure	0.51	128^2	0.0	...	0.280
N17		0.16	128^2	−0.5	...	0.193
N18		0.051	128^2	−1.0	...	0.082
N19		0.016	128^2	−1.5	...	0.023
N20		0.0051	128^2	−2.0	...	0.0078

Note. — Calculations including radiation effects have labels with prefix R. Calculations without radiation have prefix N. The initial magnetic geometry is described in § 6.1.

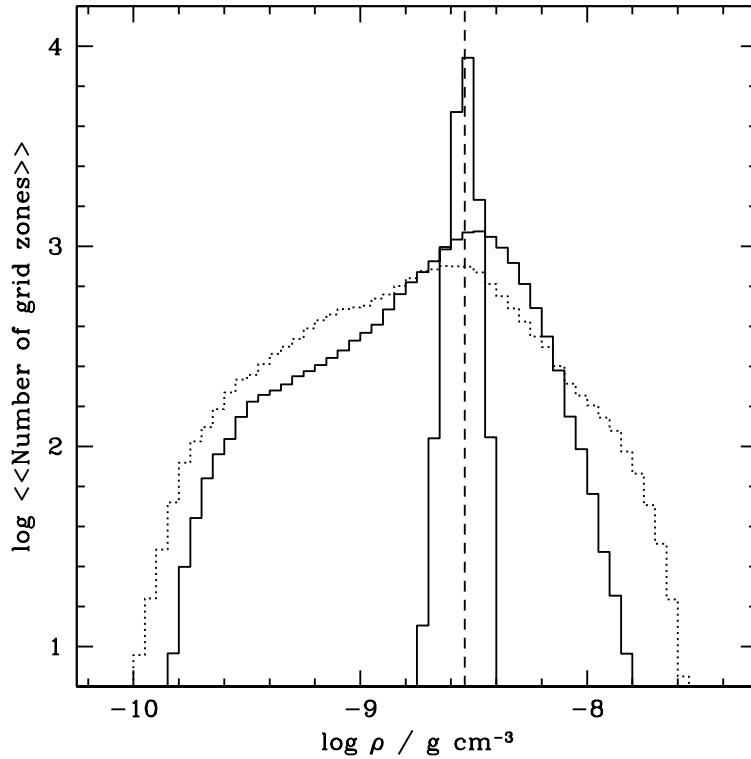


Fig. 6.— Density histograms averaged over the period from 2 to 6 orbits after the onset of turbulence. The canonical calculation R1 is indicated by a dotted line. Calculations without radiation, on the same grid and with the same initial magnetic field, are shown by solid lines. For the broader solid histogram, from calculation N11, the initial gas pressure is as in the canonical case. For the taller, narrower solid histogram, from calculation N16, initial gas pressure is larger so that total pressure matches the canonical calculation. The mean density for all three calculations is indicated by a vertical dashed line.

turbulence and the distribution of radiation evolve on the orbital timescale, while gas and radiation reach thermal equilibrium in a few timesteps. As there are about 10^4 timesteps per orbit, gas and radiation remain close to equilibrium throughout. The smaller gas temperature fluctuations in the canonical calculation are due to radiation diffusion combined with rapid thermal equilibration. Additional mechanisms for exchange of energy between material particles and radiation, such as Compton scattering, are likely to have little further effect on the temperatures. The actual equilibration time due to free-free opacity (table 1) is initially about 100 times shorter than the timestep. Its smallest local value during the turbulent stage is 14 times shorter than its initial value. Its largest is 33 times longer than the initial value. Temperature fluctuations are similar in a version of the canonical simulation R1t with Courant number reduced a factor 10, so the timesteps are closer to the true matter-radiation equilibration time.

The dense regions in the canonical calculation have lower magnetic pressure than their surroundings primarily due to weaker azimuthal fields. The radial fields in dense regions on average point towards larger x , such that differential rotation produces azimuthal fields opposing the background azimuthal field. The time average of the density-weighted mean radial field is $\langle\langle\rho B_x\rangle\rangle/\langle\rho\rangle = 1337$ G. This is comparable to the initial amplitude of the vertical component of the field, $B_0 \sin\theta = 1507$ G. In a version of the canonical calculation R1b having the sign of the initial azimuthal field reversed, fields in dense regions preferentially point towards smaller x , and the density-weighted mean radial field is -876 G. Radial magnetic field of opposite signs is partially segregated in R1 and R1b, with fields of one sign found mostly in dense regions, and those of the other sign found more often in low-density regions. The mean radial field in overdense regions, the spatial anti-correlation between gas and magnetic pressure fluctuations, the near-matches between magnetic pressure fluctuations and gas plus radiation pressure fluctuations, and the Maxwell stresses larger than the Reynolds stresses (figure 4, upper right panel) are all consistent with a picture in which the fluctuations in the gas and radiation are caused by the magnetic fluctuations.

To investigate the importance of field strength for the density fluctuations, versions of the canonical simulation are carried out with initial magnetic fields weaker by factors of $10^{0.5}$, 10, $10^{1.5}$, and 100. These are labeled R2 through R5 in table 2. The magnetic pressure is less than the gas pressure for the last three of these cases. In the weakest-field calculation R5, the ratio of gas to magnetic pressure $\beta = 120$. For each run, the height and width of the domain are reduced by the same factor as the magnetic field, so initially there are 64 zones per characteristic MRI wavelength as in the canonical simulation.

Time-averaged RMS fluctuations in the resulting turbulence are marked in figure 7 by open circles. Among the three weakest-field calculations, fluctuations in density and

pressure are proportional, as expected for isothermal perturbations. Also, the magnetic pressure fluctuations are approximately equal to the gas pressure fluctuations in each case, and the radiation pressure fluctuations are much smaller than both. For the canonical and $|\mathbf{B}| = B_0/10^{0.5}$ calculations, the density fluctuation is proportional approximately to the pressure fluctuation raised to the power 0.33.

Effects of diffusion on the density fluctuations are explored using a parallel series of calculations R6 through R10, with scattering opacity 100 times larger. Results from these runs are shown in figure 7 by filled circles. The break between slopes unity and 0.33 is at a characteristic MRI wavelength 10 times smaller than in the standard-opacity series. In both cases, the break occurs where the initial characteristic wavelength is approximately equal to the distance radiation diffuses in an orbit. The effective equation of state is isothermal for fluctuations weaker than the break point, and markedly stiffer for stronger fluctuations. The large density fluctuations observed in the canonical calculation require both a large ratio of magnetic to gas pressure, and a sufficiently high rate of radiation diffusion.

6.3. Heating Mechanisms

Radiation energy density increases with time in the canonical calculation, as shown in figure 4. The mean heating rate from 2 to 6 orbits after the onset of turbulence is similar to the dissipation rate $\frac{3}{4}\Omega_0\alpha(P + p)$ assumed in the steady-state viscous disk model of § 3. In this section we consider the sources of the heating in the canonical calculation.

The overall energy balance for gas plus radiation is obtained by adding equations 3 and 4 and integrating over the domain. Since the boundaries are periodic and the transport terms and $\nabla \cdot \mathbf{F}$ term conserve total energy, these terms integrate to zero, leaving

$$\frac{\partial}{\partial t} \langle E + e \rangle = - \langle p \nabla \cdot \mathbf{v} \rangle - \langle \nabla \mathbf{v} : \mathbf{P} \rangle. \quad (12)$$

Under optically-thick conditions as in the canonical run, the radiation pressure tensor is isotropic and the final term reduces to $-\langle P \nabla \cdot \mathbf{v} \rangle$. When radiation pressure is much larger than gas pressure, the radiation compression term dominates. Throughout the turbulent phase in the canonical calculation, the compression heating rate given by equation 12 is about an order of magnitude larger than the domain-averaged rate of heating due to the shock-capturing artificial viscosity. Integrated from 2 to 6 orbits after turbulence begins, the compression terms and artificial viscosity increase the total heat content $\langle E + e \rangle$ by 10.4% and 0.8% of the initial value, respectively. The viscous heating rate assumed in the α -disk model of § 3 corresponds to an increase in heat content by 6.3% over the same period.

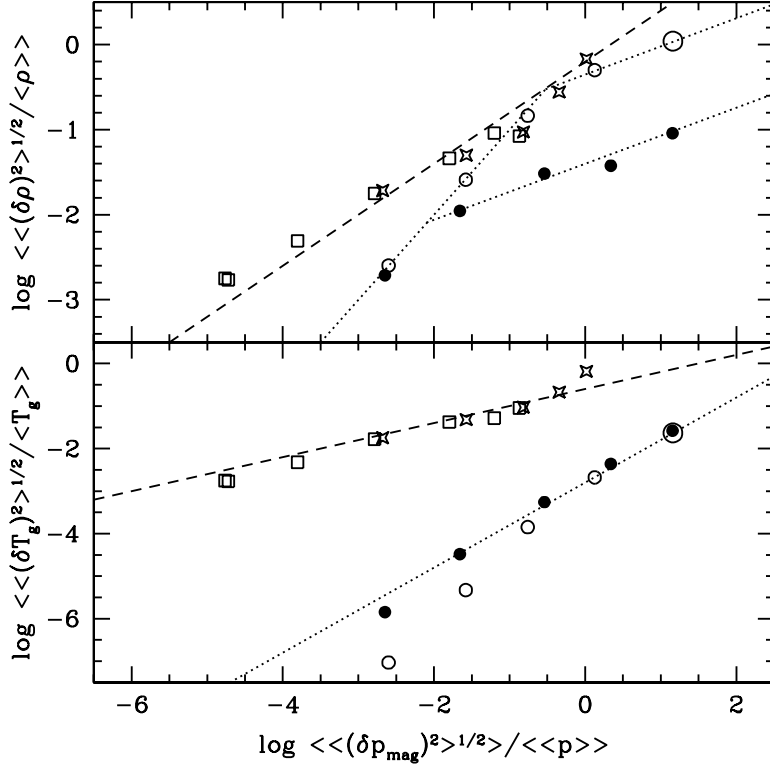


Fig. 7.— Dependence of the RMS fluctuations in density (upper) and gas temperature (lower) on the RMS magnetic pressure fluctuation in calculations with various initial field strengths. The magnetic pressure fluctuation is measured relative to the gas pressure. The fluctuations and gas pressure are time-averaged over the period from 2 to 6 orbits after the onset of turbulence. Calculations R1-R5 with radiation and the standard opacities are marked by open circles. The largest open circle represents the canonical simulation R1. Calculations R6-R10 with scattering opacity 100 times larger are indicated by filled circles. Runs without radiation N11-N15 having the same initial gas pressure are marked by stars. Those N16-N20 having the same initial total pressure are marked by squares. In the upper panel, the steepest dotted line indicates the unit slope expected for isothermal fluctuations, and the other two dotted lines have slope 0.33. Dashed lines indicate the slopes 0.6 (upper) and 0.4 (lower) expected for adiabatic fluctuations. The dotted line in the lower panel has unit slope.

Compression heating in the canonical run is fast enough to be considered as a possible mechanism for converting released gravitational energy to photons.

In the double-resolution version of the canonical calculation R1d2, the corresponding increases due to the compression terms and the artificial viscosity are 10.5% and 1.6%. In a version R1v with artificial viscosity ten times smaller, they are 6.8% and 0.098%. The amount of compression heating changes little with resolution and with the artificial viscosity. In these cases as in the canonical run, the rate of heating due to $-(P + p)\nabla \cdot \mathbf{v}$ is typically greatest where material is compressed onto the boundaries of dense regions, as shown in figure 8. In contrast, in the calculation N11 with the same initial gas pressure without radiation, the time-integrated contributions of compression and artificial viscosity are 4.1% and 1.4% of the initial total energy in the canonical calculation, respectively. In the calculation N16 with the same total pressure without radiation, the contributions are 1.6% and 0.7%. In the two calculations without radiation, the compression heating rate is most often large in the interiors of dense regions.

Pressure is more strongly anti-correlated with velocity divergence in the canonical calculation than in the versions lacking radiation effects. Anti-correlation indicates gas plus radiation pressure is larger during compression than during expansion. Redistribution of the internal energy occurs by diffusion of radiation after compression. The difference in average total pressure $P + p$ between regions of converging and diverging flow is 19.2×10^5 dyn cm⁻² in calculation R1, 3.36×10^5 dyn cm⁻² in calculation N11, and 8.82×10^5 dyn cm⁻² in calculation N16.

The importance of diffusion in separating radiation from gas is shown by the almost-uniform radiation pressure in the canonical calculation, and by the pressure-density relations plotted in figure 9. In the canonical run, radiation pressure is nearly independent of density except at the highest densities, while gas pressure is proportional to density. In the calculations N11 and N16 without radiation, the relationships between pressure and density are consistent with adiabatic evolution together with artificial viscous heating.

The time-integrated compression heating depends strongly on magnetic pressure. It exceeds the heating due to artificial viscosity only in the calculations R1 through R3 with total magnetic pressure similar to or larger than gas pressure. Compression heating is also less when the fluid is more nearly opaque. In a version of the canonical simulation R1s with a larger scattering opacity $\sigma = 10^4 \sigma_{\text{es}}$, the integrated compression heating is 1.6% and artificial viscous heating is 0.7% of the initial total energy density. These are about the same as in the calculation N16 without radiation having the same initial total pressure. We conclude that radiation damping is associated with density excursions, and occurs under the conditions outlined at the end of § 6.2. For rapid compression heating, magnetic pressure must be at

least comparable to gas pressure, and the radiation diffusion time not much longer than the time for evolution of the turbulence.

6.4. Field Geometry and Accretion Stress

Here we examine the effects of different initial magnetic field orientations on the accretion stress. In the canonical calculation, the total stress time-averaged from 2 to 6 orbits after the start of turbulence is 1.6 times the value $\alpha(P + p)$ assumed in the initial disk model of § 3. The stress which accompanies the early part of the turbulent stage is roughly consistent with the starting conditions used.

In a version of the canonical run R21, the azimuthal component of the field is reduced to the same amplitude as the vertical component. The total magnitude of the field is reduced to $|\mathbf{B}| = B_0/10$, and the field angle θ in equations 9-11 is set to 90° . As in the canonical run, the energy in the azimuthal component of the field remains roughly constant during the turbulent stage, while the energy in the vertical and radial components declines through numerical dissipation. Averaged from 2 to 6 orbits after the onset of turbulence, the pressures in the components of the magnetic field are in the ratio $\langle B_x^2 \rangle : \langle B_y^2 \rangle : \langle B_z^2 \rangle = 4.8 : 248 : 1$ in the canonical simulation, and $2.1 : 7.1 : 1$ in the simulation with weaker azimuthal field. In these axisymmetric calculations, the initial magnetic geometry affects the orientation of the field in the turbulent stage.

For both of these calculations R1 and R21, the domain- and time-averaged magnetic accretion stress $\langle \langle -B_x B_y / 4\pi \rangle \rangle$ is a few times the average pressure in the vertical component of the magnetic field. The stress due to correlated hydrodynamic fluctuations $\langle \langle \rho v_x \delta v_y \rangle \rangle$ is a few times smaller than the magnetic stress. Similar ratios between the two stresses and the z -magnetic pressure occur in weaker azimuthal field, $\theta = 90^\circ$ versions of calculations R3 and R5. These are listed as R23 and R25 in table 3. Field strength and domain size are smaller than in R21 by factors of 10 and 100, respectively. Similar ratios of the stresses are also found in each of the simulations with and without radiation listed in table 2. The accretion stresses in these calculations vary little with the azimuthal field, the gas pressure, and the radiation pressure. The stresses are proportional to the mean energy in the vertical field.

In the weaker azimuthal field calculations, as in the simulations R1 through R5 with the canonical magnetic geometry, the compression terms $-(P + p)\nabla \cdot \mathbf{v}$ are the major source of heating when magnetic pressure in the turbulent stage is greater than gas pressure. At a given ratio of magnetic to gas pressure, the ratio of the net compression heating to the

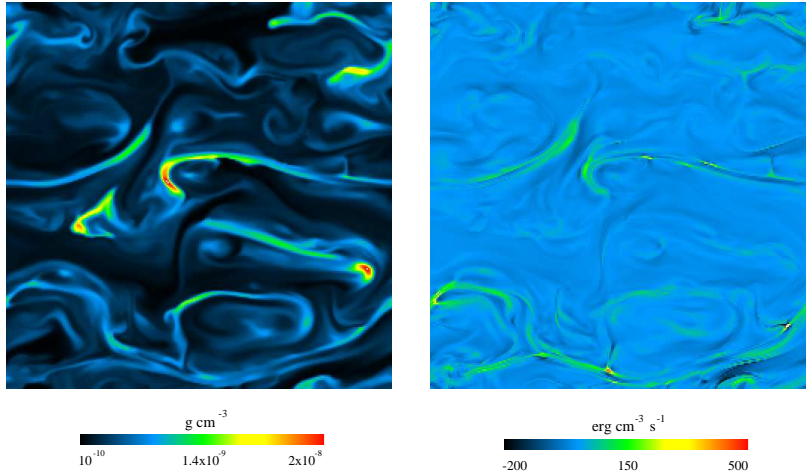


Fig. 8.— Snapshots of the density (left) and compression heating rate $-(P+p)\nabla \cdot \mathbf{v}$ (right), three orbits after turbulence begins in the double-resolution version of the canonical simulation, R1d2. The scale for the density is logarithmic, and that for the heating rate is linear. Compression heating is most commonly rapid in layers surrounding regions of high density.

Table 3. Simulations at location A with weaker azimuthal field.

Label	Name	$L/(2H)$	Zones	$\log \mathbf{B} /B_0$	$\log \langle \langle \rho_{\max}/\rho_{\min} \rangle \rangle$
R21	Weaker- B_y	0.51	128^2	-1.0	0.96
R23		0.051	128^2	-2.0	0.18
R25		0.0051	128^2	-3.0	0.0027

Note. — The initial magnetic geometry is described in § 6.4.

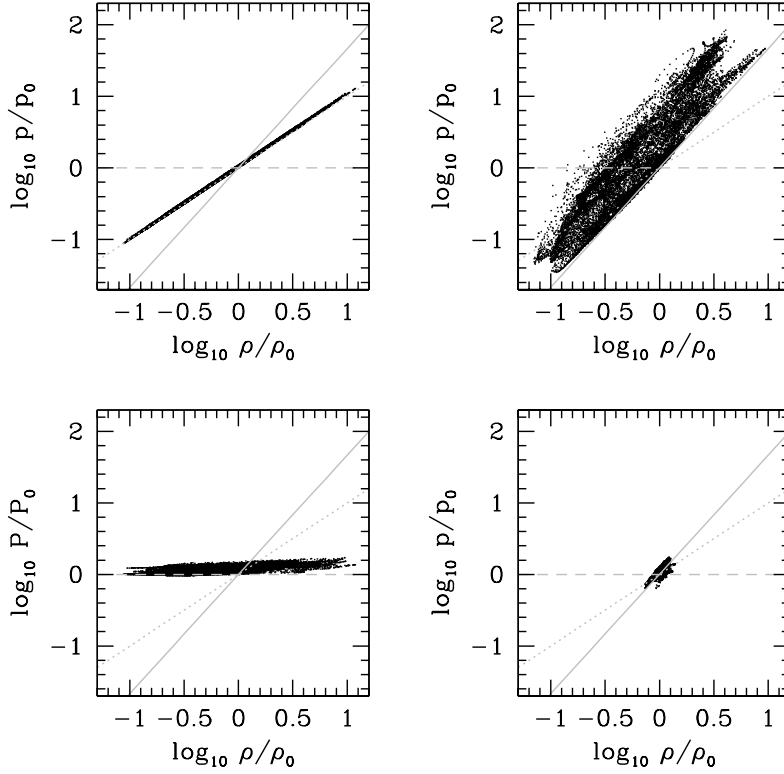


Fig. 9.— Gas pressure (upper left) and radiation pressure (lower left) versus density in the canonical calculation R1; and gas pressure versus density in the calculations without radiation having the same initial gas pressure (N11, upper right) and the same initial total pressure (N16, lower right). Conditions in all 128^2 zones are shown 2 orbits after the onset of turbulence. Each quantity is plotted on a logarithmic scale, in units of its initial value. Grey lines indicate the initial pressures (dashed) and the paths for disturbances of the initial conditions which are adiabatic (solid) and isothermal (dotted).

vertical magnetic pressure increases with the mean strength of the azimuthal field, indicating that the amount of heating depends on the geometry of the field as well as its strength.

6.5. Reduced Absorption Opacity

In radiation-dominated disks there may exist circumstances where the time for exchange of energy between gas and radiation is similar to or longer than the orbital period. To examine how disequilibrium might affect turbulence driven by the MRI, we carry out a version of the canonical calculation with absorption opacity 10^6 times lower, so that $t_{\text{eqm}} \approx 2\pi/\Omega_0$. The initial conditions and orbital frequency are identical to those used in the canonical simulation.

The turbulent stage in this calculation lasts from 4.1 orbits to about 20 orbits. During the most vigorous period of turbulence the domain-averaged gas temperature climbs, reaching 5 times the initial equilibrium temperature after 5.9 orbits. In this period, heating of the gas by $-p\nabla \cdot \mathbf{v}$ and artificial viscosity is faster than the cooling due to net emission of radiation. After 8 orbits the gas temperature declines, and from 15 orbits onwards it is close to the radiation temperature. Over the turbulent stage, the radiation temperature increases gradually by a total of 6%. At its largest, the domain-averaged gas pressure is 5.8% of the initial radiation pressure. The smallest point-by-point ratio of radiation to gas pressure is 1.5, and some parts of the flow are only marginally radiation-dominated during the most vigorous turbulence. The average RMS density fluctuation from 2 to 6 orbits after the onset of turbulence is 54%, somewhat less than in the canonical calculation. Gas temperature is almost uniform in the canonical run. In the version with reduced absorption opacity the RMS gas temperature fluctuation is roughly equal to the density fluctuation from the onset of turbulence until 12 orbits, and then decreases. The RMS radiation temperature fluctuation is near one-thirtieth of the density fluctuation for the whole of the turbulent stage, as radiation diffusion remains effective.

In similar low-absorption-opacity versions of the weaker-field calculations R3 and R5, the domain-averaged gas temperature differs little from the radiation temperature. The time-averaged RMS gas temperature fluctuations are intermediate between the gas temperature fluctuations observed without radiation in runs N11-N20 and those in the standard-opacity calculations R1-R5.

Overall, the lower absorption opacity leads to decoupling of gas and radiation temperatures during the part of the turbulent stage when heating is most rapid. The density fluctuations, stress, and total heating are little different from those in the versions of the

canonical calculation with the same initial magnetic fields.

6.6. Ratio of Gas to Radiation Pressure

The results of the earlier parts of this section indicate that radiation effects may be important at locations where radiation pressure greatly exceeds gas pressure. In this final part we consider whether radiation effects are significant when gas and radiation pressures are comparable. Under these conditions, magnetic pressure is unlikely to be much larger than gas pressure. A version of the canonical calculation is carried out using the initial mass and energy densities and orbital frequency found at location B in the disk model of § 3. The domain size is unchanged at 51% of the thickness of the initial disk model. Field strength is chosen so the Alfvén speed is equal to the gas and radiation acoustic speeds, and the pressures of the radiation, magnetic field, and gas are in the ratio 1.25 : 0.833 : 1. The number of orbits required for photons to diffuse vertically through the disk is independent of radius in the radiation-dominated α -prescription, so L^2/D is 50 orbits here as in the canonical calculation.

Time-averaged from 2 to 6 orbits after the start of turbulence, the RMS density fluctuation is 12%, an order of magnitude smaller than in the canonical calculation. The largest density on the grid during this period is on average 2.3 times the smallest density. The time-averaged RMS temperature fluctuation is 0.7%, about one-third that in the canonical calculation. The time-averaged RMS gas pressure fluctuation is 85% of the magnetic pressure fluctuation, suggesting radiation pressure support of fluctuations is less important than in the canonical simulation.

Gas plus radiation energy density increases between 2 and 6 orbits after the start of turbulence by 5.2% due to compression, and by 1.2% due to artificial viscosity. The compression heating is comparable to the viscous dissipation assumed in the initial disk model at location B. The dissipation in that model corresponds to an increase by 8.1% over the same time. As in the canonical calculation, the compression heating rate is largest in layers near the boundaries between dense and underdense regions. Overall, the density and temperature fluctuations are weaker under these conditions than at location A, and the compression heating rate in units of $(E + e)\Omega_0$ is about half as great. The time-averaged total accretion stress is 0.61 times the viscous stress $\alpha(P + p)$ assumed in the initial disk model at location B. This ratio is several times lower than observed in the canonical run at location A.

In additional calculations with the field strength and grid spacing both reduced, by factors of 10 in one case and 100 in the other, the turbulence is almost exactly isothermal and

incompressible, and no compression heating is detected. The three location B calculations are listed in table 4.

7. DISCUSSION

To understand the luminous output of accretion disks around compact objects we would like to know, given a certain rate of delivery of material to the outer edge of the radiation-dominated region, how the gas, radiation, and magnetic pressures are distributed in the interior. Some processes which are likely to determine these quantities are angular momentum transfer, magnetic dynamo action, dissipation and buoyant losses of field, outflows, heating of the disk material, and losses of radiation through the disk surfaces.

7.1. Magnetic Gains and Losses

Magnetic energy increases in the present calculations through differential orbital motion, and decreases through work done on the gas and through numerical dissipation involving grid-scale averaging of opposing fields. The results obtained in § 6 suggest that magnetic fields may influence the gas and radiation by transporting angular momentum outwards and driving turbulence leading to heating. The gas and radiation are likely to alter the fields in turn through effects of compressibility and buoyancy. The calculations performed here cannot be used to learn about the evolution of this coupled system because the stratification is neglected, and the axisymmetry restricts field amplification to a period of a few orbits, which is less than the thermal timescale for the disk. However, the association described in § 6.2 between overdense regions and radial magnetic field of one sign raises the possibility of a negative feedback. Regions with net radial field tend to produce strong azimuthal field through shear. Fluctuations with the opposite radial field are compressed in this background, and are more likely to sink towards the midplane because of their greater density. Over time, such buoyancy effects might favor removal of the original net radial field to the disk surface layers.

In radiation-dominated disks at locations where vertical gravity is important, magnetic losses due to buoyancy might be enhanced by diffusion of radiation from the surroundings into rising, expanding magnetized regions (Parker 1975; Stella & Rosner 1984). The hard X-ray spectra of a range of objects powered by accretion onto black holes indicate Comptonization in hot coronae of low optical depth (Zdziarski 1999). The coronae may be heated by dissipation of magnetic fields (Merloni & Fabian 2000). Magnetized coronae have been

observed to form in simulations of a local patch of accretion disk extending several scale heights above and below the midplane (Miller & Stone 2000).

7.2. Radiation Gains and Losses

In the calculations of § 6, turbulence is driven on scales near the characteristic MRI wavelength. When magnetic pressure is larger than gas pressure, the turbulence is highly compressible, and some of its kinetic energy is converted to photon energy through a radiative damping similar to the process described for linear MHD waves by Agol & Krolik (1998). As in the linear analysis, larger or denser regions are less compressible because radiation diffuses from them more slowly. In smaller or less-dense regions, diffusion makes radiation pressure gradient forces ineffective. Damping is strongest in the simulations in layers near the boundaries between regions of high and low density. The layers have transverse lengths comparable to the MRI wavelength, and thicknesses typically a few percent of the scale height of the α -disk model from which the initial conditions were selected. The combination of density and thickness is such that radiation diffuses through the damping layers in about an orbital period.

Dissipation of kinetic energy in the simulations follows three paths. Work is done in compressing the radiation directly, and in compressing the gas. Kinetic energy is also converted to gas internal energy through the artificial viscous heating used to numerically capture shocks. In the canonical calculation the rate at which $-P\nabla \cdot \mathbf{v}$ work is done on the radiation is much greater than the rate at which $-p\nabla \cdot \mathbf{v}$ work is done on the gas, since radiation pressure is initially 125 times gas pressure. The time- and domain-averaged rate of artificial viscous heating is about 10% of the sum of the two compression heating rates. The majority of the energy deposited in the gas is converted to photons within a few timesteps. For the location A initial state, thermal equilibrium requires that linear increases in energy density are partitioned 1000 : 1 between radiation and gas.

In the interiors of real accretion disks, energy lost by dissipation of magnetic fields is likely released as heat. This effect is not included in the present ideal-MHD calculations, where energy lost through numerical dissipation of the field vanishes with no corresponding heating. In the canonical calculation between 2 and 6 orbits after turbulence begins, the decrease in magnetic energy is less than one tenth the increase in radiation energy density due to compression heating. We conclude that radiative damping of compressive motions could be an important heating mechanism in radiation-dominated disks.

In the picture developed by Shakura & Sunyaev (1973), density varies hardly at all

between the midplane and the disk surfaces, and radiation is lost by diffusion. The results outlined in § 6.2 indicate that if the magnetic field exceeds equipartition with the gas, and radiation diffuses an MRI wavelength in about an orbit, much of the disk material may be compressed into small dense regions by magnetic activity. Under these conditions radiation would likely be lost from the disk at an increased rate. The time- and domain-averaged radiation diffusion rate $\langle\langle D \rangle\rangle / L^2$ during the turbulent stage in the canonical calculation is about twice the rate in the uniform initial condition. The radiation flux in an atmosphere with density inhomogeneities may exceed the Eddington flux, with low-density regions pushed up by radiation while high-density regions are pulled down by gravity (Shaviv 1998; Begelman 2001). The clumpy state of the canonical calculation during the turbulent stage differs from the two-phase equilibrium proposed by Krolik (1998) in having densities continuously distributed around a single most-common value (figure 6). The clumps here are formed, confined, and destroyed by the magnetic field, and have lifetimes around one orbital period. We have included neither the magnetic dissipation heating and Compton cooling which might establish a long-lived hot phase, nor the thermal conduction which might set the size of cold-phase clumps.

Large-scale buoyancy effects, which may enhance the overall cooling rate, do not appear in our calculations since the vertical component of gravity is neglected. Ordinary convection might prove as effective as diffusion in cooling a radiation-dominated α -disk (Agol et al. 2001). Although stratification is not included here, the photon bubble instability (Gammie 1998) could be present locally where turbulent accelerations have components parallel to the radiation flux. For sufficiently large fluxes, linear photon bubble modes with wavelengths somewhat shorter than the MRI characteristic wavelength can grow faster than the MRI (Blaes & Socrates 2001). However the similarities in gas and magnetic fluctuations between the canonical simulation R1 and the simulation without radiation having the same initial gas pressure, N11, suggest the resolved wavelengths of the photon bubble instability are not important in this instance. It is unclear how well convective and photon bubble modes grow under sustained vertical gravity in a background of turbulence driven by the MRI.

8. CONCLUSIONS

We performed axisymmetric radiation MHD simulations of the MRI in local patches of a radiation-dominated accretion disk, neglecting the vertical component of gravity. On initially-uniform magnetic fields with a strong azimuthal component, radiation diffusion reduced the growth rates of the linear modes in detailed agreement with the analysis by Blaes & Socrates (2001). On initially vertical fields, the non-linear development of the

instability led to channel solutions in which compression of the dense layers was hastened by diffusive loss of radiation pressure support. On magnetic fields with zero net vertical flux, the non-linear development resulted in about ten orbits of decaying turbulence. Because these axisymmetric calculations showed no sustained dynamo action, the results cannot be used to learn the steady-state strength of the magnetic field. When magnetic pressure was bigger than gas pressure and the distance that radiation diffused in an orbit was at least comparable to the characteristic MRI wavelength, density contrasts as large as the ratio of magnetic to gas pressure were driven by magnetic forces. Overdense regions were destroyed and reformed in the turbulence about once per orbit. Diffusion of radiation out of the compressed regions led to partial separation of gas and radiation. In cases with the standard free-free and electron scattering opacities, the gas remained in good thermal contact with the radiation, and both were approximately isothermal. The flow was heated by radiation damping of compressive turbulent motions. Heating was fastest in regions where the compression rate and radiation diffusion rate were similar. Angular momentum was transported outwards by a total accretion stress approximately four times the pressure in the vertical component of the magnetic field. At fixed vertical field strength, the stress showed little dependence on the gas and radiation pressures. The accretion stresses and heating rates in calculations with initial magnetic pressure comparable to radiation pressure were similar to the viscous stresses and dissipation rates assumed in the α -disk model used to select the initial conditions. Strong clumping of the gas occurring at such magnetic pressures might allow more rapid cooling of radiation-dominated disks than in the commonly assumed case of uniform density.

This work was supported by the United States Department of Energy under grant DFG-0398-DP-00215, and benefited from our discussions with E. Agol, S. Balbus, O. Blaes, R. Blandford, R. Bowers, J. Cannizzo, C. Gammie, J. Hawley, W.-T. Kim, J. Krolik, M. C. Miller, E. Ostriker, and A. Socrates. A. Young kindly made computer time available.

REFERENCES

- Agol, E., & Krolik, J. 1998, *ApJ*, 507, 304
- Agol, E., Krolik, J., Turner N. J., & Stone, J. M. 2001, *ApJ*, 558, 543
- Balbus, S. A., & Hawley, J. F. 1991, *ApJ*, 376, 214
- Balbus, S. A., & Hawley, J. F. 1998, *Rev. Mod. Phys.* 70, 1
- Begelman, M. C. 2001, *ApJ*, 551, 897

- Blaes, O. M., & Balbus, S. A. 1994, *ApJ*, 421, 163
- Blaes, O. M., & Socrates, A. 2001, *ApJ*, 553, 987
- Brandenburg, A., Nordlund, Å., Stein, R. F., & Torkelsson, U. 1995, *ApJ*, 446, 741
- Fabian, A. C., Iwasawa, K., Reynolds, C. S., & Young, A. J. 2000, *PASP*, 112, 1145
- Gallimore, J. F., Baum, S. A., O’Dea, C. P., Brinks, E., & Pedlar, A. 1996, *ApJ*, 462, 740
- Gammie, C. F. 1998, *MNRAS*, 297, 929
- Goodman, J., & Xu, G. 1994, *ApJ*, 432, 213
- Greenhill, L. J., Moran, J. M., & Herrnstein, J. R. 1997, *ApJ*, 481, L23
- Hawley, J. F., & Balbus, S. A. 1991, *ApJ*, 376, 223
- Hawley, J. F., & Balbus, S. A. 1992, *ApJ*, 400, 595
- Hawley, J. F., Gammie, C. F., & Balbus, S. A. 1995, *ApJ*, 440, 742
- Hawley, J. F., Gammie, C. F., & Balbus, S. A. 1996, *ApJ*, 464, 690
- Hubeny, I., Blaes, O., Krolik, J. H., & Agol, E. 2001, *ApJ*, 559, 680
- Kim, W.-T., & Ostriker, E. C. 2000, *ApJ*, 540, 372
- Krolik, J. H. 1998, *ApJ*, 498, L13
- Levermore C. D., & Pomraning G. C. 1981, *ApJ*, 248, 321
- Merloni, A., & Fabian, A. C. 2000, *MNRAS*, 321, 549
- Mihalas, D., & Mihalas, B. W. 1984, *Foundations of Radiation Hydrodynamics* (Oxford: Oxford Univ. Press)
- Miller, K. A., & Stone, J. M. 2000, *ApJ*, 534, 398
- Mirabel, I. F., & Rodriguez, L. F. 1999, *ARA&A*, 37, 409
- Miyoshi, M., Moran, J., Herrnstein, J., Greenhill, L., Nakai, N., Diamond, P., & Inoue, M. 1995, *Nature*, 373, 127
- Orosz, J. A., & Bailyn, C. D. 1997, *ApJ*, 477, 876
- Parker, E. N. 1975, *ApJ*, 198, 205

- Parmar, A. N., White, N. E., Giommi, P., & Gottwald, M. 1986, *ApJ*, 308, 199
- Shakura, N. I., & Sunyaev, R. A. 1973, *A&A*, 24, 337
- Shaviv, N. J. 1998, *ApJ*, 494, L193
- Stella L., & Rosner R. 1984, *ApJ*, 277, 312
- Stone, J. M., Hawley, J. F., Gammie, C. F., & Balbus, S. A. 1996, *ApJ*, 463, 656
- Stone, J. M., & Norman, M. L. 1992a, *ApJS*, 80, 753
- Stone, J. M., & Norman, M. L. 1992b, *ApJS*, 80, 791
- Stone, J. M., Mihalas, D., & Norman, M. L. 1992, *ApJS*, 80, 819
- Tanaka, Y., et al. 1995, *Nature*, 375, 659
- Turner, N. J., & Stone, J. M. 2001, *ApJS*, 135, 95
- von Neumann, J., & Richtmyer, R. D. 1950, *J. Appl. Phys.*, 21, 232
- Zdziarski, A. A. 1999, *ASP Conference Series* vol. 161, eds J. Poutanen & R. Svensson, p. 16

Table 4. Simulations at location B with strong azimuthal field

Label	Name	$L/(2H)$	Zones	$\log \mathbf{B} /B_0$	$\log \langle \langle \rho_{\max}/\rho_{\min} \rangle \rangle$
R31	Location B	0.51	128^2	0.0	0.37
R33		0.051	128^2	-1.0	0.0077
R35		0.0051	128^2	-2.0	6.9×10^{-5}

Note. — The initial magnetic geometry is described in § 6.1.